Vacancy enhanced oxygen redox reversibility in P3-type magnesium doped sodium manganese oxide $Na_{0.67}Mg_{0.2}Mn_{0.8}O_2$

Eun Jeong Kim,[†,#,^] Le Anh Ma,[§] David M. Pickup,[‡] Alan V. Chadwick,[‡] Reza Younesi,[§,#] Philip Maughan,[†,^] John T.S. Irvine,[†,^] A. Robert Armstrong[*,†,#,^]

[†]School of Chemistry, University of St Andrews, St Andrews, KY16 9ST, United Kingdom

[#] ALISTORE-ERI, 80039, Amiens Cedex, France

[^]The Faraday Institution, Quad One, Harwell Science and Innovation Campus, Didcot, OX11 0RA, United Kingdom

[§]Ångström Advanced Battery Centre, Department of Chemistry Ångström Laboratory, Uppsala University, Uppsala, SE-75121, Sweden

[‡]School of Physical Sciences, University of Kent, Canterbury, CT2 7NH, United Kingdom

ABSTRACT

Lithium-rich layered oxides and sodium layered oxides represent attractive positive electrode materials exhibiting excess capacity delivered by additional oxygen redox activity. However, structural degradation in the bulk and detrimental reactions with the electrolyte on the surface often occur, leading to limited reversibility of oxygen redox processes. Here we present the properties of P3-type $Na_{0.67}Mg_{0.2}Mn_{0.8}O_2$ synthesized under both air and oxygen. Both materials exhibit stable cycling performance in the voltage range 1.8-3.8 V where the Mn^{3+}/Mn^{4+} redox couple entirely dominates the electrochemical reaction. Oxygen redox activity is triggered for both compounds in the wider voltage window 1.8-4.3 V with typical large voltage hysteresis from non-bonding O 2p states generated by substituted Mg. Interestingly, for the compound prepared under oxygen, an additional novel reversible oxygen redox activity is shown with exceptionally small voltage hysteresis (20 mV). The presence of vacancies in the transition metal layers is shown to play a critical role not only in forming unpaired O 2p states independent of substituted elements but also in stabilising the P3 structure during charge with reduced structural transformation to the O'3 phase at the end of discharge. This study reveals the important role of vacancies in P3-type sodium layered oxides to increase energy density using both cationic and anionic redox processes.

KEYWORDS

Sodium ion batteries, Positive electrode materials, P3 structure, Transition metal vacancies, Oxygen redox

INTRODUCTION

Since the redox reaction of oxygen ions was revealed as an alternative approach to increase the capacity of Li-rich layered oxides, extensive studies have been carried out to establish the mechanism of oxygen redox in lithium ion batteries (LIBs). The knowledge gained from LIB research has been translated to sodium ion batteries (SIBs) assisting the fundamental understanding of oxygen redox in SIBs. However, far more studies are required to draw a complete picture of the charge compensation mechanism driven by oxygen in SIBs as a result of the range of different polymorphs adopted by sodium layered oxides.

As counterparts of Li-rich layered oxides, O3-type Na-rich oxides such as $Na[Na_{1/3}Ru_{2/3}]O_2$[1] and $Na[Na_{1/3}Ir_{2/3}]O_2$[2] (square brackets represent transition metal layers) have been explored and have shown oxygen redox activity based on the strong hybridization between O 2p and the 4d or 5d states of the transition metals. Among 3d transition metal based compounds, several studies on P2-type sodium manganese based oxides ($Na_xM_yMn_{1-y}O_2$ where x ≈ 0.7 and M= Li, Mg, Fe, Ni, Zn and mixtures of elements) have shown that appropriate substitution can produce non-bonding O 2p states which are responsible for oxygen redox.[3–9] A few studies on P3-type sodium manganese based oxides, for example $Na_{0.6}Li_{0.2}Mn_{0.8}O_2$,[10,11] $Na_{2/3}Mg_{1/3}Mn_{2/3}O_2$[12] and $Na_{0.67}Ni_{0.2}Mn_{0.8}O_2$[13] have also suggested the contribution of oxygen ions.

In the majority of compounds exhibiting oxygen redox, there are issues such as large voltage hysteresis, oxygen loss from the lattice, irreversible structural change and cationic migration from the transition metal layers.[14–17] To overcome these problems, stabilizing labile oxygen whilst retaining the layered structure is required. Recently, Bruce and co-workers[18] reported that oxygen coordinated by three cations in the transition metal layers is essential to stabilize the labile oxygen avoiding oxygen loss upon desodiation in P2-type materials. In addition, the important role of vacancies in the transition metal layers for the reversibility of oxygen redox was highlighted by Yamada and co-workers.[19] The inherent vacancies in $Na_{4/7}[\square_{1/7}Mn_{6/7}]O_2$ (empty square represents vacancies in Mn sites) permit stable oxygen redox with exceptionally small voltage hysteresis retaining the rigid layered structure over several cycles.[19] Li *et al.* also reported reversible oxygen redox in $Na_{4/7}[\square_{1/7}Mn_{6/7}]O_2$ with a robust structure without migration of Mn cations.[20] Later, Song *et al.* reported that the small polarization of oxygen redox in $Na_{4/7}[\square_{1/7}Mn_{6/7}]O_2$ originates from the well-maintained oxygen stacking sequence without irreversible structural change and cationic migration from transition metal layers to Na ion layers.[21]

The beneficial effects of transition metal vacancies on the oxygen redox in $Na_{4/7}[\square_{1/7}Mn_{6/7}]O_2$ inspired us to stabilize labile oxygen via vacancies in the transition metal layers of compounds adopting the P3-

type structure which show the same oxygen stacking (ABBCCA…) as $Na_{4/7}[\square_{1/7}Mn_{6/7}]O_2$. In this report, P3-type $Na_{0.67}Mg_{0.2}Mn_{0.8}O_2$ was synthesized under different atmospheres and cooling rate in order to vary the concentration of vacancies in the transition metal layers. Two compounds prepared under different synthetic conditions exhibit stable cycling performance in the voltage window 1.8-3.8 V where Mn^{3+}/Mn^{4+} redox chemistry is responsible for charge compensation. In the extended voltage range where oxygen redox is triggered, a new reversible plateau is found with very small polarization in the compound with 4% vacancies on the Mn sites induced by more oxidizing synthetic conditions. In contrast, the compound without Mn vacancies only exhibits large voltage hysteresis and limited reversibility of the oxygen redox. The presence of in-plane vacancies also permits retention of the P3 structure upon charge and reduced structural transformation to the O'3 phase at the end of discharge.

EXPERIMENTAL SECTION

A stoichiometric amount of sodium carbonate (Na_2CO_3, Fisher Chemistry, ≥ 99.5 %) was dissolved in deionized water (solution A). A separate aqueous solution of magnesium acetate tetrahydrate ($Mg(CH_3CO_2)_2 \cdot 4H_2O$, Sigma-Aldrich, 99 %) and manganese (II) acetate tetrahydrate ($Mn(CH_3CO_2)_2 \cdot 4H_2O$, Sigma-Aldrich, ≥ 99 %) was prepared (solution B). The solution A was added dropwise to solution B under stirring then stirred for a further 15 min. The water was removed using a rotary evaporator. The resulting solid was heated to 300 °C at a rate of 6 °C min^{-1} for 12 h and cooled to 50 °C at a rate of 6 °C min^{-1}. The powder was then ground and heated again to 625 °C at a rate of 5 °C min^{-1} for 3 h under air and quenched; the obtained sample is denoted Air-$Na_{0.67}Mg_{0.2}Mn_{0.8}O_2$. Alternatively, the decomposed powder was ground and heated to 625 °C at a rate of 5 °C min^{-1} for 3 h under oxygen then cooled to 50 °C at a rate of 5 °C min^{-1} to obtain Oxy-$Na_{0.67}Mg_{0.2}Mn_{0.8}O_2$. The as-synthesized materials were stored in an Ar-filled glovebox.

Powder X-ray diffraction (PXRD) patterns of as-synthesized compounds were recorded on a PANalytical Empyrean diffractometer in Bragg-Brentano geometry with Cu $K\alpha_1$ radiation (λ = 1.5406 Å). The obtained patterns were indexed by the Le Bail method using the GSAS package with the EXPGUI interface.[22] Structures were refined by the Rietveld method using Topas Academic v6.[23] Thermal parameters were constrained to typical values for this class of material. Occupancies were refined for the sodium sites and the sites in the transition metal layer with a variety of models being tested. Scanning electron microscopy (SEM) images of as-synthesized materials were recorded on a JEOL JSM-6700F. Inductively coupled plasma optical emission spectroscopy (ICP-OES) analysis was performed using a PerkinElmer Optima 8300 and a iCAP 6000 Series for Air-$Na_{0.67}Mg_{0.2}Mn_{0.8}O_2$ and Oxy-$Na_{0.67}Mg_{0.2}Mn_{0.8}O_2$, respectively. Mn K-edge X-ray absorption near edge structure (XANES) spectra were collected in transmission mode at the beamline B18 at the Diamond Light source. Reference

spectra were collected for each measurement using Mn metal foil. At least three scans were taken for each sample and the data were merged, calibrated, background subtracted and normalized using the program Athena. X-ray photoelectron spectroscopy (XPS) analysis for Air-$Na_{0.67}Mg_{0.2}Mn_{0.8}O_2$ was carried out using a PHI 5500 system with monochromatic aluminum K_α X-ray source (1487 eV photon energy). This corresponds to a depth of analysis of approximately 15 nm determined by the inelastic mean free path of polyethylene.[24] The obtained data were plotted using the software Igor Po 6.34A. All peaks were calibrated based on the hydrocarbon species C 1s peak at 285 eV.

In order to evaluate the electrochemical performance of the materials, slurries were prepared using the active material (Air-$Na_{0.67}Mg_{0.2}Mn_{0.8}O_2$ or Oxy-$Na_{0.67}Mg_{0.2}Mn_{0.8}O_2$), super C65 carbon and Solef 5130 binder (a modified polyvinylidene fluoride (PVDF)) in the mass ratio 75: 15: 10 in in n-methyl-2-pyrrolidone, which was then cast on aluminum foil using a doctor blade. After drying, 12 mm diameter electrode discs were punched then dried at 80 °C under vacuum for 12 h. Typical cast electrode loadings were 2.6 mg cm^{-2}. Preparation of the slurries was carried out in air within 6 hrs. CR2325 coin cells were assembled in an Ar-filled glovebox and used for evaluation of electrochemical performance. The cells consisted of a disc electrode, sodium metal as a counter/reference electrode, a glass fiber separator (Whatman, GF/F) and the electrolyte (1M $NaClO_4$ in propylene carbonate containing 3 % fluoroethylene carbonate by weight). Galvanostatic charge/discharge cycling and voltage scans (linear sweep voltammetry) were carried out at 30 °C using a Maccor Series 4200 battery cycler. To prepare electrochemically cycled Air-$Na_{0.67}Mg_{0.2}Mn_{0.8}O_2$ and Oxy-$Na_{0.67}Mg_{0.2}Mn_{0.8}O_2$ for *ex-situ* characterization, working electrodes were constructed by mixing the active material (Air-$Na_{0.67}Mg_{0.2}Mn_{0.8}O_2$ or Oxy-$Na_{0.67}Mg_{0.2}Mn_{0.8}O_2$) and super C65 carbon in the mass ratio 75: 25 with no binder in air. The mixture was dried at 110 °C under vacuum for 12 h and was used as electrodes. Typical powder electrode loadings were 24.5 mg cm^{-2}. For *ex-situ* XPS for Air-$Na_{0.67}Mg_{0.2}Mn_{0.8}O_2$, CR2325 coin cells were assembled as described above except that Solupor membranes replaced the glass fiber separator. For all *ex-situ* measurements except the XPS, Swagelok-type cells were assembled in an Ar-filled glovebox. The cells consisted of a desired amount of working electrode, sodium metal as a counter/reference electrode, glass fiber separators (Whatman, GF/F) and the electrolyte (1M $NaClO_4$ in propylene carbonate containing 3 % fluoroethylene carbonate by weight).

For all *ex-situ* measurements, cycled cells were transferred to an Ar-filled glovebox before opening and the active material was extracted. The electrodes were rinsed carefully with dry dimethyl carbonate to remove residual electrolyte and then left under vacuum for 12 h to ensure all solvent had evaporated. PXRD patterns of cycled materials were collected on a PANalytical Empyrean diffractometer operating in capillary mode with Mo Kα radiation (λ = 0.7107 Å). Samples were contained in 0.7 mm glass capillaries. Structures were refined by the Rietveld method using Topas

Academic v6.[23] Due to the presence of carbon and the background associated with the use of a glass capillary, the superlattice peaks are barely visible, therefore a simple P3-type structural model with the space group *R3m* was adopted. For refinements containing two layered phases the peak shapes were constrained to be the same. XANES and XPS measurements for cycled samples were carried out as described above.

RESULTS AND DISCUSSION

Characterization of as-synthesized compounds

PXRD patterns of as-synthesized Air-$Na_{0.67}Mg_{0.2}Mn_{0.8}O_2$ and Oxy-$Na_{0.67}Mg_{0.2}Mn_{0.8}O_2$ were recorded with Cu Kα_1 radiation (λ = 1.5406 Å). The major diffraction peaks of the PXRD patterns of both samples can be indexed to an ideal P3 structural model (space group *R3m*), where Na ions occupy trigonal prismatic sites while Mg and Mn ions are located in the octahedral sites in ABBCCA oxygen stacking. However, the small peaks around 20-25° are unindexed as highlighted by the blue circle in Figure S1. Similar characteristic peaks have been reported for other P2- and P3-type materials and typically arise from ordering in the transition metal layers. These peaks can be indexed on the basis of a superlattice model (space group *Cm*), in which Mg ions are in the center of a honeycomb arrangement surrounded by Mn ions (Figure 1a and 1b for Air-$Na_{0.67}Mg_{0.2}Mn_{0.8}O_2$ and Oxy-$Na_{0.67}Mg_{0.2}Mn_{0.8}O_2$, respectively). It is worth noting that the superlattice model applied in this study, (Figure 1c), represents a different setting from the previously published model[12] and trace amounts of MgO (~1.2% for Air-$Na_{0.67}Mg_{0.2}Mn_{0.8}O_2$ and 1.6% for Oxy-$Na_{0.67}Mg_{0.2}Mn_{0.8}O_2$, respectively) are found for both compounds. Refined structural results (Table S1) reveal that Oxy-$Na_{0.67}Mg_{0.2}Mn_{0.8}O_2$ contains 4% transition metal vacancies and the unit cell volume (242.59 Å^3) is smaller than that of Air- $Na_{0.67}Mg_{0.2}Mn_{0.8}O_2$ (243.74 Å^3). These results confirm successful introduction of vacancies in transition metal layers under oxygen atmosphere and slow cooling. This agrees well with previous studies carried out in our group[25–27] and other groups[28–30] showing the formation of vacancies in sodium manganese oxides under oxidising synthesis conditions.

Comparing the average valence of Mn of both compounds based on the compositions derived from refined occupancies and ICP-OES analysis (Table 1) shows that the oxidation state of Mn for Oxy-$Na_{0.67}Mg_{0.2}Mn_{0.8}O_2$ is higher regardless of analytical methods.

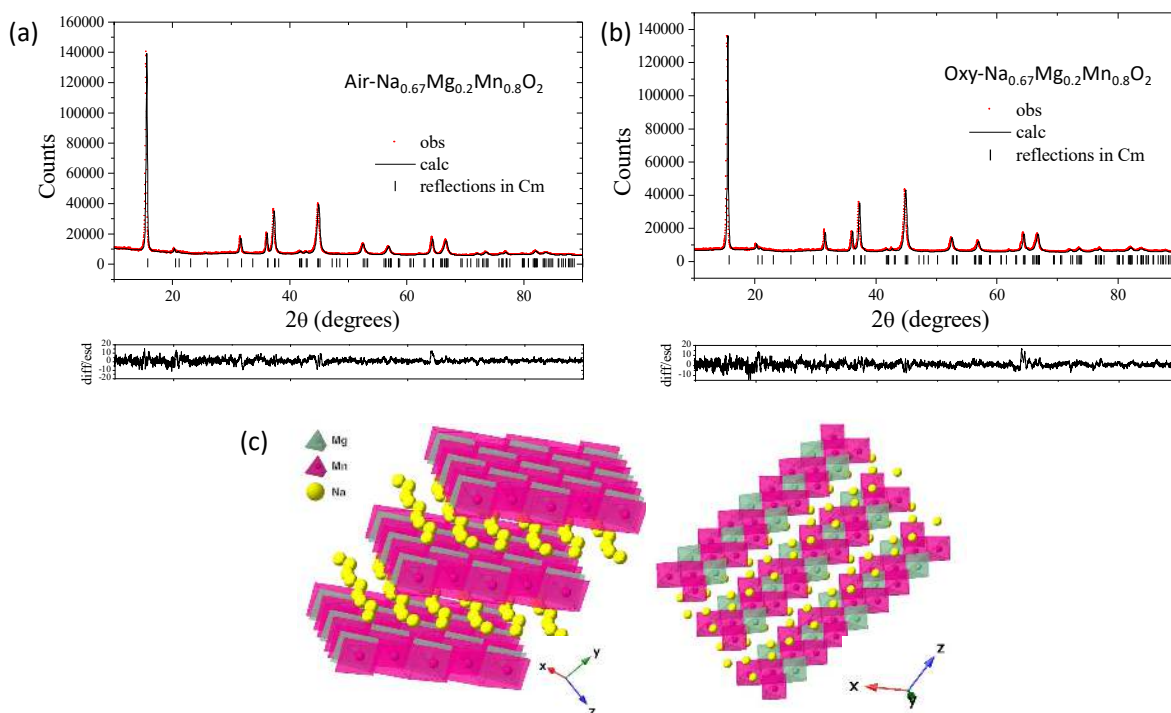Figure 1. Profile fits for as-synthesized (a) Air-$Na_{0.67}Mg_{0.2}Mn_{0.8}O_2$ and (b) Oxy-$Na_{0.67}Mg_{0.2}Mn_{0.8}O_2$ using the space group of *Cm*. Observed data points are shown in red, with fitted profile in black and the difference/esd shown below. Tick marks indicate allowed reflections for *Cm*. (c) Structural diagram of the superlattice model used in this study.

Table 1. Stoichiometric ratio and average valence of Mn derived from Rietveld refinement and ICP-OES (normalized using Mg+Mn = 1.00) for both samples.

	Rietveld refinement	ICP-OES
Air-$Na_{0.67}Mg_{0.2}Mn_{0.8}O_2$	$Na_{0.61}Mg_{0.19}Mn_{0.81}^{3.72+}O_2$	$Na_{0.67}Mg_{0.19}Mn_{0.81}^{3.64+}O_2$
Oxy-$Na_{0.67}Mg_{0.2}Mn_{0.8}O_2$	$Na_{0.67}Mg_{0.20}Mn_{0.76}^{3.86+}\square_{0.04}O_2$	$Na_{0.62}Mg_{0.21}Mn_{0.79}^{3.75+}O_2$

The morphology of as-synthesized Air-$Na_{0.67}Mg_{0.2}Mn_{0.8}O_2$ and Oxy-$Na_{0.67}Mg_{0.2}Mn_{0.8}O_2$ was characterized by SEM. The different synthetic conditions have a negligible influence on the morphology of the as-synthesised compounds which exhibit agglomerated primary particles of around 100 nm. (Figure 2)
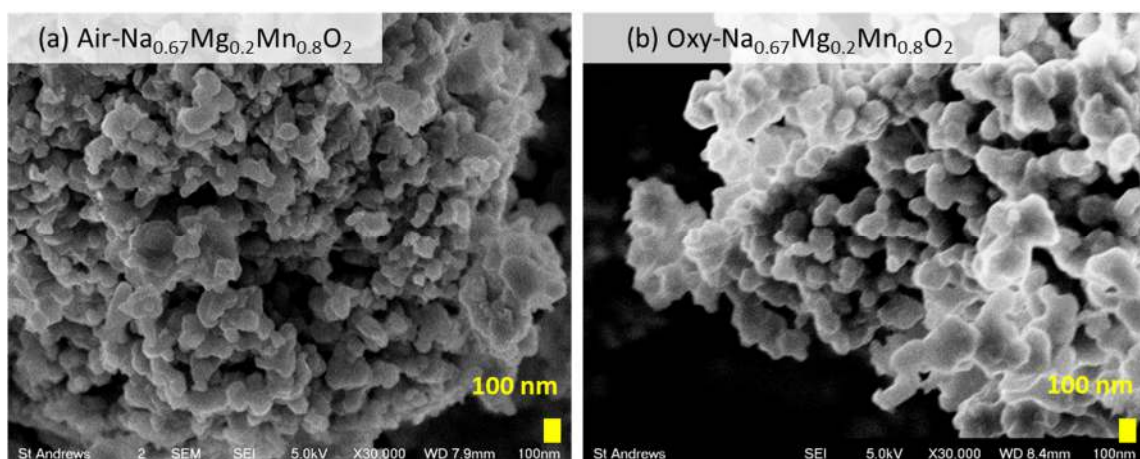
Figure 2. SEM images of as-synthesized (a) Air-$Na_{0.67}Mg_{0.2}Mn_{0.8}O_2$ and (b) Oxy-$Na_{0.67}Mg_{0.2}Mn_{0.8}O_2$.

Electrochemical properties of Air-$Na_{0.67}Mg_{0.2}Mn_{0.8}O_2$ and Oxy-$Na_{0.67}Mg_{0.2}Mn_{0.8}O_2$

Electrodes with Air-$Na_{0.67}Mg_{0.2}Mn_{0.8}O_2$ and Oxy-$Na_{0.67}Mg_{0.2}Mn_{0.8}O_2$ were prepared and the assembled coin cells were tested in two different voltage windows. Figure 3a shows their galvanostatic cycling performance cycled between 1.8 and 3.8 V. Both materials exhibit stable cycling performance, retaining around 96% of their initial discharge capacity after 25 cycles. Oxy-$Na_{0.67}Mg_{0.2}Mn_{0.8}O_2$ delivers smaller first charge capacity of 26 mAh g^{-1}, corresponding to the removal of 0.09 Na^+ compared to that of Air-$Na_{0.67}Mg_{0.2}Mn_{0.8}O_2$ (40 mAh g^{-1}, equivalent to deintercalation of 0.14 Na^+). As the electrochemical reaction is dominated by Mn redox in this voltage range, the smaller charge capacity is indicative of a lower content of Mn^{3+} in Oxy-$Na_{0.67}Mg_{0.2}Mn_{0.8}O_2$, which agrees well with the refined unit cell volume. Charge/discharge curves and the corresponding differential capacity versus voltage (dQ/dV) plots collected on the second cycle are shown in Figure 3b and Figure 3c, respectively. Both materials exhibit a smooth voltage profile thanks to the dilution of Jahn-Teller active Mn^{3+} centers with Mg^{2+} which pushes the average Mn oxidation state towards Mn^{4+}.[31] In the case of Oxy-$Na_{0.67}Mg_{0.2}Mn_{0.8}O_2$ this effect is enhanced by the introduction of vacancies. The absence of the very short plateau at around 3.5 V in Oxy-$Na_{0.67}Mg_{0.2}Mn_{0.8}O_2$ further supports the higher concentration of Mn^{4+}. Interestingly, a small plateau at around 2.0 V is found only for Air- $Na_{0.67}Mg_{0.2}Mn_{0.8}O_2$, reflected in the dQ/dV plot as a corresponding sharp redox pair (oxidation and reduction peaks at 2.0 and 1.9 V, respectively) followed by a broad oxidation (at 2.2 V) and reduction (at 2.1 V) peaks. In contrast, Oxy-$Na_{0.67}Mg_{0.2}Mn_{0.8}O_2$ only shows sharp and intense oxidation and reduction peaks at 2.2 V and 2.1 V, respectively. Since the operating voltage is strongly related to the covalency of the Mn-O bonds, the redox couple around 2.15 V for both materials can be attributed to a Mn^{4+} rich environment whereas the redox pair at 1.95 V exclusively shown in Air-$Na_{0.67}Mg_{0.2}Mn_{0.8}O_2$ might stem from the more covalent nature of Mn^{3+} in accordance with the increased concentration of Mn^{3+} in this compound.[32,33]
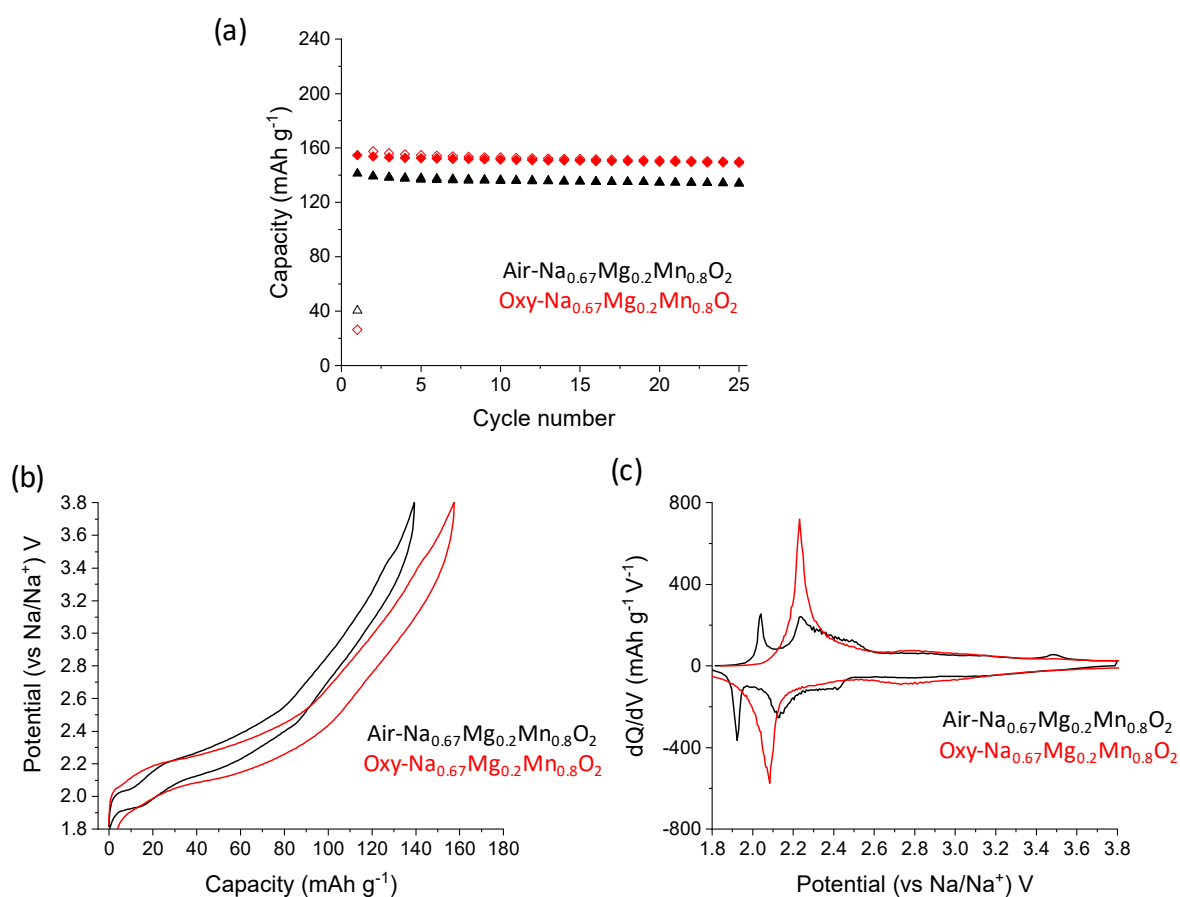
Figure 3. (a) Galvanostatic cycling performance of Air-$Na_{0.67}Mg_{0.2}Mn_{0.8}O_2$ (black) and Oxy-$Na_{0.67}Mg_{0.2}Mn_{0.8}O_2$ (red) cycled at 30 °C between 1.8 and 3.8 V at a rate of 10 mA g^{-1}. Empty and full symbols represent charge and discharge capacity, respectively. (b) Charge/discharge curves on the second cycle and (c) the corresponding dQ/dV plots for Air-$Na_{0.67}Mg_{0.2}Mn_{0.8}O_2$ (black) and Oxy-$Na_{0.67}Mg_{0.2}Mn_{0.8}O_2$ (red).

The rate performance of Air-$Na_{0.67}Mg_{0.2}Mn_{0.8}O_2$ was further investigated, fixing the voltage window at 1.8-3.8 V. As displayed in Figure 4a, excellent capacity retention is shown at rates of 10, 50 and 200 mA g^{-1}, while the capacity retention after 50 cycles is only 53 % at a rate of 500 mA g^{-1}. As the rate increases from the slow regimes (10 and 50 mA g^{-1}) to the faster regimes (200 and 500 mA g^{-1}), the discharge capacity decreases from 141 mAh g^{-1} to 107 mAh g^{-1}. This originates from incomplete sodiation on the first cycle (Figure 4b). In order to further confirm this, Air-$Na_{0.67}Mg_{0.2}Mn_{0.8}O_2$ electrodes were cycled at 200 mA g^{-1}, varying the lower cut-off voltage from 1.8 to 1.5 V. As shown in Figure S2, increased capacity is delivered over the wider voltage window. Figure 4c shows that at rates of 200 and 500 mA g^{-1}, the polarization in the charge/discharge curves on the second cycle significantly increases in the lower voltage region at high levels of sodiation, where the phase transformation to an O'3 structure is likely because of additional intercalation of Na ions (confirmed by ex-situ PXRD). It is

shown that Na diffusion in O3 and O'3 structures is slower than that in P3 because Na ions diffuse through shared faces between two adjacent prismatic sites in the P3 structure whereas Na ions pass via interstitial tetrahedral sites between two octahedral sites in the O3 structure.[34] This suggests that the increased polarization in Air-$Na_{0.67}Mg_{0.2}Mn_{0.8}O_2$ at faster rates might arise from the sluggish migration of Na ions in the O'3 structure. This limited Na ion kinetics becomes more obvious at cycle 50 where the low voltage process is inaccessible at the highest rate (Figure 4d). In the case of the cell cycled at 500 mA g^{-1}, not only the incomplete sodiation but also the sluggish reactions caused by the phase transformation (P3 to O'3) as well as limited kinetics in the O'3 phase are responsible for the capacity fade. The enlarged polarization is also observed in Oxy-$Na_{0.67}Mg_{0.2}Mn_{0.8}O_2$ cycled at 200 mA g^{-1} (Figure S3) since the phase transition to O'3 also occurs (confirmed by ex-situ PXRD) whilst slightly higher initial capacity is delivered than Air-$Na_{0.67}Mg_{0.2}Mn_{0.8}O_2$ consistent with the results at 10 mA g^{-1}.
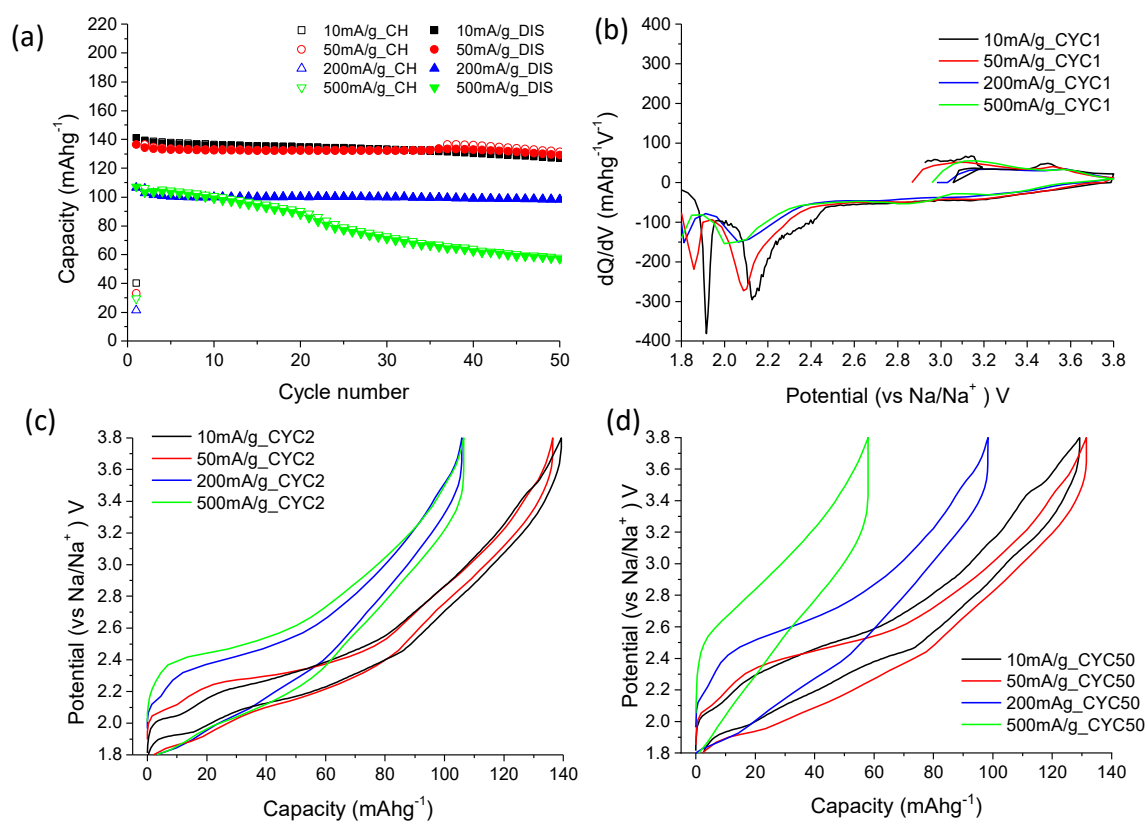

Figure 4. (a) Galvanostatic cycling performance of Air-$Na_{0.67}Mg_{0.2}Mn_{0.8}O_2$ cycled at 30°C between 1.8 and 3.8 V at a rate of 10 mA g^{-1} in black, 50 mA g^{-1} in red, 200 mA g^{-1} in blue and 500 mA g^{-1} in green. Empty and full symbols represent charge and discharge capacity, respectively, (b) dQ/dV plots for the first cycle, Charge/discharge curves for (c) the second cycle and (d) 50th cycle.

In order to activate oxygen redox an extended voltage window of 1.8 to 4.3 V was investigated. As shown in Figure 5a, the increased upper cut-off voltage delivers larger capacity but results in reduced

capacity retention for both Air-$Na_{0.67}Mg_{0.2}Mn_{0.8}O_2$ and Oxy-$Na_{0.67}Mg_{0.2}Mn_{0.8}O_2$. Charge/discharge curves on the first cycle and the corresponding dQ/dV plots are presented in Figure 5b and 5c, respectively. When the compounds are charged to 4.3 V, both compounds exhibit a plateau beyond 4.0 V on the first charge. Upon subsequent discharge, no obvious plateau is found for Air-$Na_{0.67}Mg_{0.2}Mn_{0.8}O_2$ while Oxy-$Na_{0.67}Mg_{0.2}Mn_{0.8}O_2$ shows a reversible plateau at 4.2 V with small polarization (Figure 5b). This contrast is clearly reflected in the dQ/dV plots on the first cycle (Figure 5c) where an irreversible peak is observed at ca. 4.15 for Air-$Na_{0.67}Mg_{0.2}Mn_{0.8}O_2$ whereas an additional reversible oxidation peak at 4.22 V coupled with a reduction peak at 4.2 V is found for Oxy-$Na_{0.67}Mg_{0.2}Mn_{0.8}O_2$. In addition, the reversible process solely observed in Oxy-$Na_{0.67}Mg_{0.2}Mn_{0.8}O_2$ is maintained over several cycles as shown in Figure 5d. Due to the instability of the electrolyte in the high voltage region and/or side reactions between the active material and decomposed electrolyte products, the reversible oxygen redox is limited but clearly observed on the second cycle (Figure S4a). It is challenging to quantify the exact discharge capacity as a function of the redox source because the discharge process of the oxygen redox associated with Mg doping occurs at around 2.7 V where Mn^{3+}/Mn^{4+} redox also occurs. Instead, we compared how much discharge capacity is delivered by the oxygen redox in the high voltage region (3.8 – 4.3 V, region in magenta in Figure S5) among the total reversible capacity originated from the oxygen redox and certain amount of the Mn redox (2.7 – 3.8 V, region in violet in Figure S5). The results reveal that 9% and 5% of discharge capacity originate from only the oxygen redox for Oxy-$Na_{0.67}Mg_{0.2}Mn_{0.8}O_2$ and Air-$Na_{0.67}Mg_{0.2}Mn_{0.8}O_2$, respectively. This agrees well with the presence of 4% vacancies in Oxy-$Na_{0.67}Mg_{0.2}Mn_{0.8}O_2$ and confirms that the vacancies are an additional source of the oxygen redox in Oxy-$Na_{0.67}Mg_{0.2}Mn_{0.8}O_2$. The ratio of discharge capacity from Mn redox (1.8 – 2.7 V, region in cyan) to the sum of the Mn redox and oxygen redox (2.7 – 3.8 V, region in violet) was also calculated. Oxy-$Na_{0.67}Mg_{0.2}Mn_{0.8}O_2$ delivers 30% capacity from the Mn redox within the voltage range of 1.8 – 2.7 V while the Mn redox provides 35% discharge capacity in Air-$Na_{0.67}Mg_{0.2}Mn_{0.8}O_2$. Again, this result is consistent with the presence of transition metal vacancies in Oxy-$Na_{0.67}Mg_{0.2}Mn_{0.8}O_2$. In the low voltage region, both materials display a plateau at 2.1 V upon discharge, which persists on subsequent cycles (Figure S4b and 5d for Air-$Na_{0.67}Mg_{0.2}Mn_{0.8}O_2$ and Oxy-$Na_{0.67}Mg_{0.2}Mn_{0.8}O_2$, respectively). Interestingly, the reversible plateau observed at 1.95 V for Air-$Na_{0.67}Mg_{0.2}Mn_{0.8}O_2$ (Figure 3c) cycled over the narrow voltage window (1.8 – 3.8 V) disappears, implying rearrangements of electronic and/or local structure associated with oxygen redox.
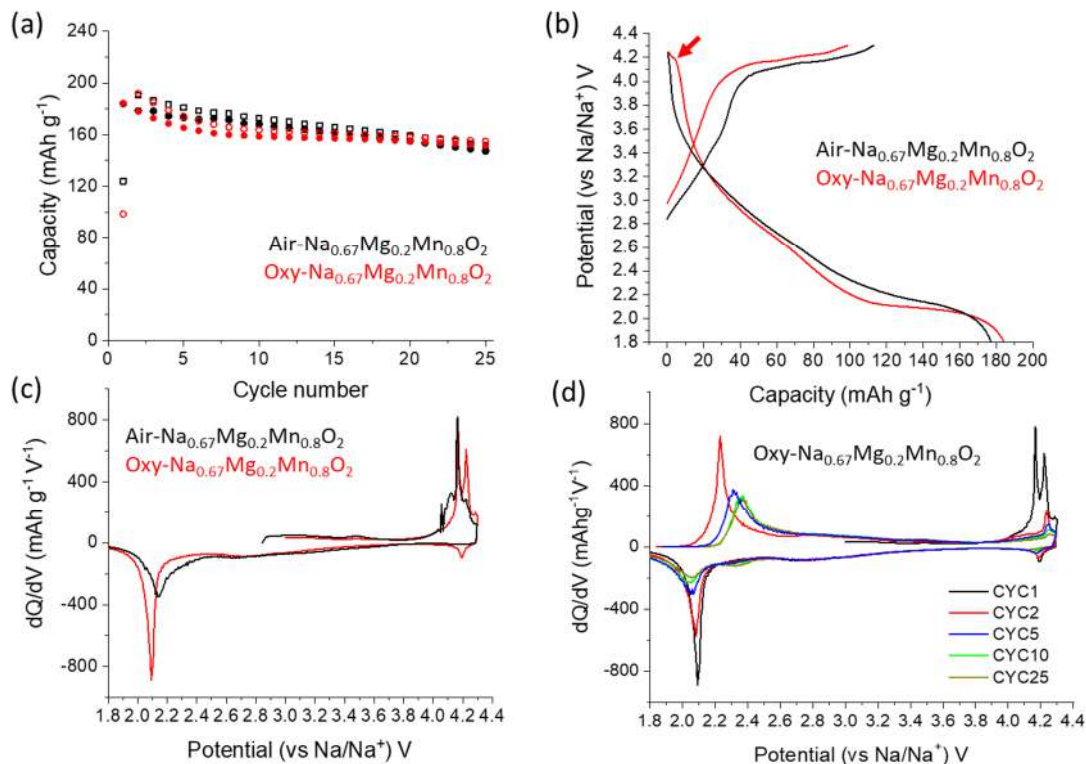
Figure 5. (a) Galvanostatic cycling performance of Air-$Na_{0.67}Mg_{0.2}Mn_{0.8}O_2$ (black) and Oxy-$Na_{0.67}Mg_{0.2}Mn_{0.8}O_2$ (red) cycled at 30 °C between 1.8 and 4.3 V at a rate of 10 mA g^{-1}. Empty and full symbols represent charge and discharge capacity, respectively. (b) Charge/discharge curves on the first cycle for Air-$Na_{0.67}Mg_{0.2}Mn_{0.8}O_2$ (black) and Oxy-$Na_{0.67}Mg_{0.2}Mn_{0.8}O_2$ (red) with an arrow indicating reversible oxygen redox and (c) the corresponding dQ/dV plots for Air-$Na_{0.67}Mg_{0.2}Mn_{0.8}O_2$ (black) and Oxy-$Na_{0.67}Mg_{0.2}Mn_{0.8}O_2$ (red). (d) dQ/dV plots corresponding to cycle 1 (black), cycle 2 (red), cycle 5 (blue), cycle 10 (green) and cycled 30 (dark yellow) for Oxy-$Na_{0.67}Mg_{0.2}Mn_{0.8}O_2$.

It has been shown that a large voltage hysteresis may be associated with migration of the substituted element from the transition metal layers.[8,12] Recently, it was reported that honeycomb ordering in the transition metal layer favors in-plane migration of Mn, leading to a lower discharge voltage associated with oxygen redox.[35] Given that honeycomb ordering is present and Mg is substituted for Mn in both Air-$Na_{0.67}Mg_{0.2}Mn_{0.8}O_2$ and Oxy-$Na_{0.67}Mg_{0.2}Mn_{0.8}O_2$, it is reasonable that the in-plane migration of Mn and/or the partially reversible Mg motion between transition metal and Na ion layers may occur in the high voltage region, resulting in a large voltage hysteresis for oxygen redox. In order to clarify the discharge voltage associated with oxygen redox, a series of cyclic voltammograms was collected by applying a progressively higher positive potential with a scan rate of 30 μV s^{-1} from OCV to upper cut-off voltages at 3.3, 3.8 and 4.3 V, fixing the lower cut-off voltage at 1.8 V for each cycle. For Air-$Na_{0.67}Mg_{0.2}Mn_{0.8}O_2$ (Figure 6a), two reduction peaks at around 1.9 and 2.1 V are observed on the first cycle where the positive potential was applied from OCV to 3.3 V followed by negative potential to

1.8 V. On the subsequent cycle, two oxidation peaks at ca. 2.1 and 2.3 V are observed with the corresponding reduction peaks at around 1.9 and 2.1 V, overlapping with those of the first cycle (Mn^{3+}/Mn^{4+} redox). On the following cycle, the oxidation peak at about 4.25 V is coupled to a small and broad reduction peak at about 2.7 V, confirming the low discharge voltage and large hysteresis associated with oxygen redox. In the case of Oxy-$Na_{0.67}Mg_{0.2}Mn_{0.8}O_2$ (Figure 6b), the Mn^{3+}/Mn^{4+} redox at the lowest voltage is significantly smaller, while the oxidation and reduction peak at 2.3 and 2.1 V, respectively, dominates below 3.8 V. By enlarging upper cut-off voltage, a new oxidation peak emerges at 4.25 V which is accompanied by two reduction peaks at 4.2 and 2.7 V, arising from oxygen redox. The voltammetric analysis not only validates the reduced discharge voltage of oxygen redox but also suggests an additional novel mechanism of oxygen redox exclusively found in Oxy-$Na_{0.67}Mg_{0.2}Mn_{0.8}O_2$.

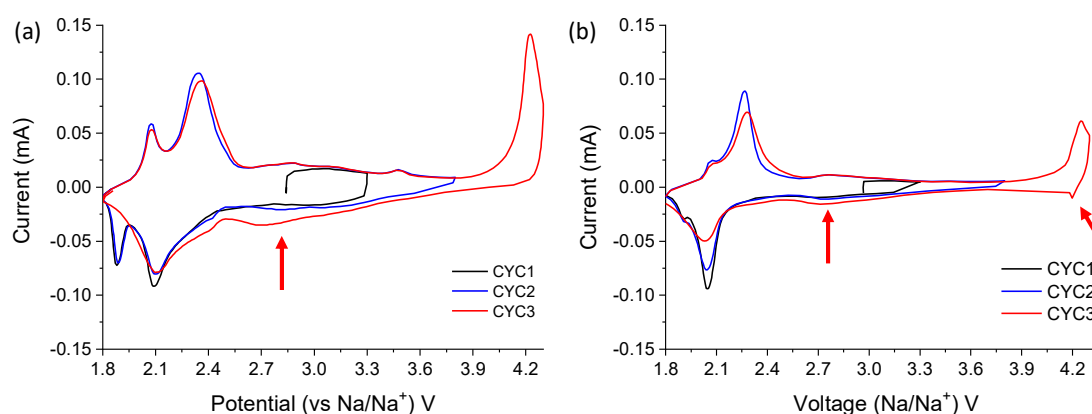Figure 6. Voltammetric analysis for (a) Air-$Na_{0.67}Mg_{0.2}Mn_{0.8}O_2$ and (b) Oxy-$Na_{0.67}Mg_{0.2}Mn_{0.8}O_2$ at a scan rate of 30 μV s^{-1}. Red arrows represent reduction peaks associated with oxygen redox.

Evolution of electronic structure for Air-Na$_{0.67}$Mg$_{0.2}$Mn$_{0.8}$O$_2$

In order to confirm oxygen redox in the high voltage region, the evolution of the oxidation state of Mn was investigated. XANES measurements were carried out at the Mn K-edge for Air-Na$_{0.67}$Mg$_{0.2}$Mn$_{0.8}$O$_2$ extracted at the end of charge and discharge, cycled over two different voltage windows as shown in Figure 7a. The collected Mn K-edge XANES spectra are presented in Figure 7b. The Mn valence for individual samples was calculated from the position of the centroid of the pre-edge (Figure 7d) relative to those from standard references, Mn$_2$O$_3$ and MnO$_2$.[36] Qualitatively comparing the standard references with the spectrum of the as-synthesized material, the pristine sample contains predominantly Mn^{4+} with a minor presence of Mn^{3+}. The quantitatively determined Mn valence for the pristine sample based on the pre-edge fitting (3.80 ± 0.15) agrees with that deduced by refined occupancies (3.72) and ICP-OES analysis (3.64) within error. After charge to 3.8 V (3.8CH), the inflection point of the spectrum shifts subtly toward higher energy (Figure 7c), indicating oxidation of the residual Mn^{3+}. Further charge to 4.3 V (4.3CH) shows no evidence of a significant shift, reflecting no contribution from the Mn to charge compensation (Figure 7c). At the end of discharge following charge to 3.8 V (3.8CYC) and 4.3 V (4.3CYC), the shape and edge position of the XANES spectra are essentially identical and shift towards lower energy, representing Mn reduction. These results provide indirect evidence of the participation of oxygen in the charge compensation mechanism beyond 3.8 V for Air-Na$_{0.67}$Mg$_{0.2}$Mn$_{0.8}$O$_2$, giving rise to a long plateau above this voltage. Promoting further oxidation of Mn with the creation of in-plane vacancies under more oxidizing synthetic conditions is demonstrated by the XANES spectrum of as-prepared Oxy-Na$_{0.67}$Mg$_{0.2}$Mn$_{0.8}$O$_2$ of which the inflection point is nearly overlapped with that of Air-Na$_{0.67}$Mg$_{0.2}$Mn$_{0.8}$O$_2$ after charge to 3.8 V and 4.3 V where the Mn oxidation state is nearly tetravalent (Figure S6). Our study on P3-type materials with different dopants shows that the evolution of Mn valence is unaffected beyond 3.8 V by the presence of transition metal vacancies.[37,38] Therefore, a long plateau observed in both compounds on the first charge indicates the participation of oxygen in the charge compensation.
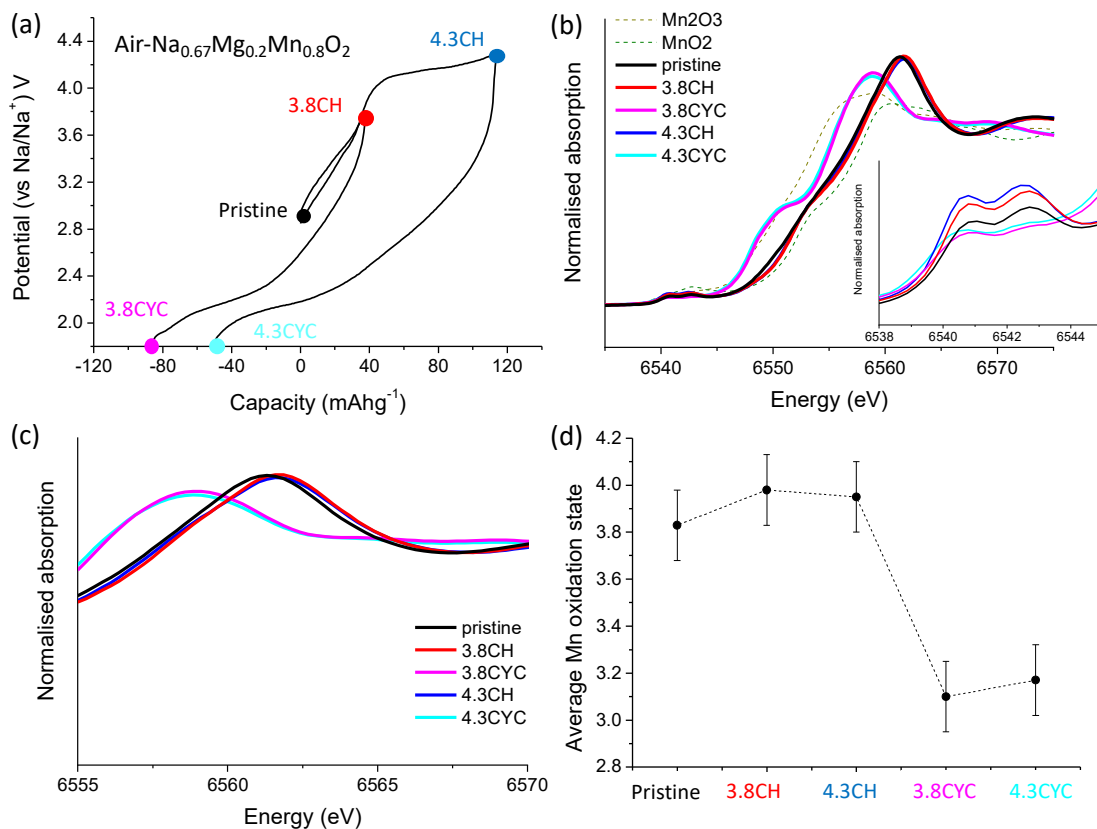
Figure 7. (a) Galvanostatic cycling curves recorded at 10 mA g^{-1} for Air-Na$_{0.67}$Mg$_{0.2}$Mn$_{0.8}$O$_2$ cycled at 30 °C in the two voltage windows: 1.8-3.8 V and 1.8-4.3 V with the points where XANES, XPS and PXRD were conducted. (b) Mn K-edge XANES spectra of the *ex-situ* Air-Na$_{0.67}$Mg$_{0.2}$Mn$_{0.8}$O$_2$ compared with reference of Mn^{3+} (Mn$_2$O$_3$) and Mn^{4+} (MnO$_2$) with an inset for the pre-edge (c) zoom of the main peak of the absorption edge, ascribed to the transition of 1s to 4p states and (d) Variation of Mn oxidation state, calculated from the position of the centroid of the pre-edge.

Surface study for Air-Na$_{0.67}$Mg$_{0.2}$Mn$_{0.8}$O$_2$

One of the main reasons for the capacity fade often observed for oxygen redox active materials is detrimental reactions with the electrolyte in the high voltage region.[15,39] In order to address this matter, XPS measurements were performed for the extracted samples at different states of charge for Air-Na$_{0.67}$Mg$_{0.2}$Mn$_{0.8}$O$_2$ and the collected XPS spectra for Mn 2p, O 1s and C 1s regions are shown in Figure 8. The Mn 2p spectra (Figure 8a) show the surface changes on the electrode Air-Na$_{0.67}$Mg$_{0.2}$Mn$_{0.8}$O$_2$. Two peaks at 643 and 655 eV can be assigned to Mn 2p$_{3/2}$ and Mn 2p$_{1/2}$, respectively.[40] There are no significant changes when the material is charged to 3.8 V. In contrast, the intensity of the spectra of 4.3 CH and 4.3 CYC is reduced, which might originate from the deposit of electrolyte decomposition products on the active material particle surface. Due to the high signal/noise ratio in the Mn 2p spectra, the oxidation state of Mn cannot be identified. The O 1s spectrum of the as prepared electrode shows

a component at 530 eV, which is characteristic of O^{2-} in the crystal lattice (Figure 8b).[41] An additional peak at 532 eV can be attributed to Na_2CO_3, often present in layered sodium transition metal oxides, and/or surface adsorbed species.[9,42] Two more components at 534 and 535 eV, corresponding to C-O and O=C-O chemical environments, are present for all electrodes exposed to the electrolyte. The contribution of these components is substantial especially for the 4.3 CH and 4.3 CYC samples. In the C 1s spectra (Figure 8c), super C65 mainly contributes to the peak at 285 eV, attributed to C-C and C-H components. The peak at 291 eV can be assigned to C-F in the PVDF backbone and CO_3^{2-} carbon environments. Two additional components at 286.5 and 289 eV, which can be attributed to the C-O and O=C-O components, respectively, are gradually enhanced for the samples charged to 4.3 V. This observation is consistent with those in the O 1s spectra. The electrolyte decomposition observed in Air-$Na_{0.67}Mg_{0.2}Mn_{0.8}O_2$ is also expected to occur in Oxy-$Na_{0.67}Mg_{0.2}Mn_{0.8}O_2$ since a major driving force of the decomposition is electrochemical instability of the electrolyte in the high voltage region.[43]
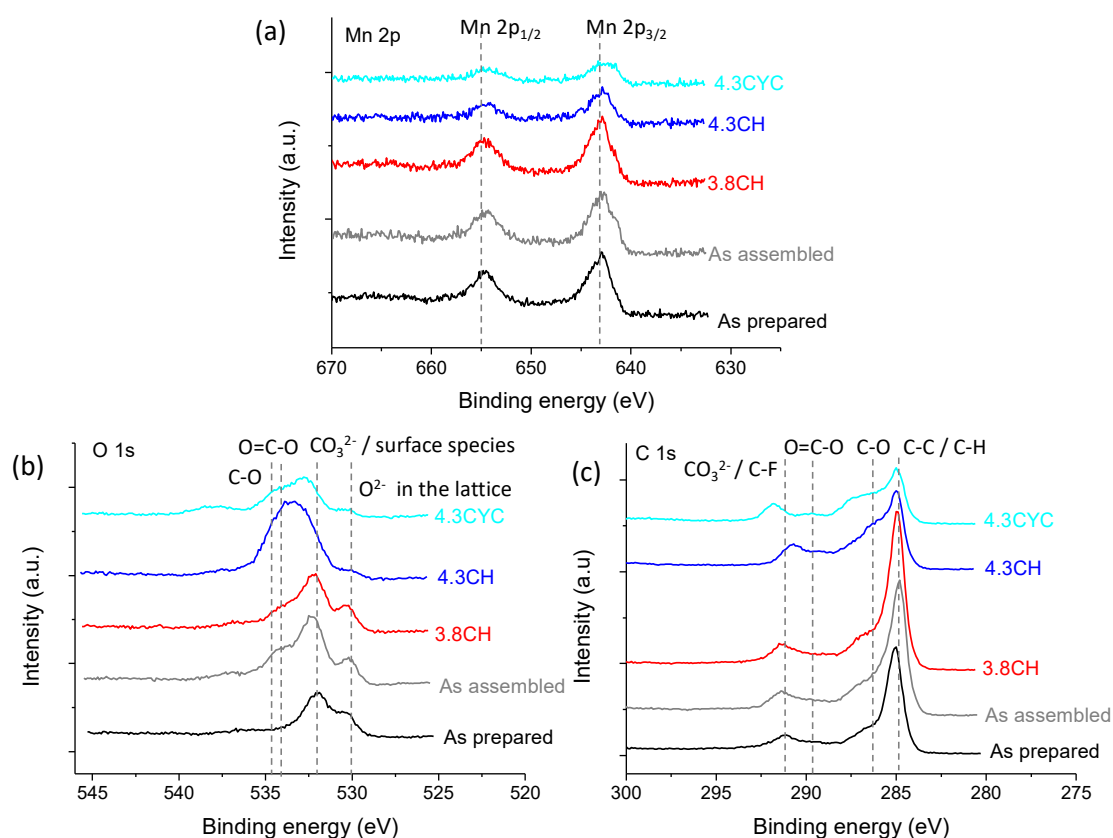

Figure 8. XPS spectra in (a) Mn 2p, (b) O 1s and (c) C 1s regions.

Structural evolution upon cycling Air-$Na_{0.67}Mg_{0.2}Mn_{0.8}O_2$ and Oxy-$Na_{0.67}Mg_{0.2}Mn_{0.8}O_2$

The presence of transition metal vacancies has been shown not only to promote crystal structure retention[19,21] but also diminish the number of stacking faults by self-ordering during oxygen redox.[1,44] In order to investigate the structural evolution of Air-$Na_{0.67}Mg_{0.2}Mn_{0.8}O_2$ and Oxy-$Na_{0.67}Mg_{0.2}Mn_{0.8}O_2$, *ex-situ* PXRD measurements were carried out for both compounds. The refined profile fits using the Rietveld method are shown in Figure 9 and the refined structural results are presented in Tables S2 and S3 for Air-$Na_{0.67}Mg_{0.2}Mn_{0.8}O_2$ and Oxy-$Na_{0.67}Mg_{0.2}Mn_{0.8}O_2$, respectively. Due to the presence of carbon and the background associated with the use of a glass capillary, the superlattice peaks are barely visible, therefore a simple P3-type structural model with the space group *R3m* was adopted. Since oxygen loss does not occur in the Mg-doped P2 system and is reported to occur very gradually on extended cycling in P3 $Na_{2/3}Mg_{1/3}Mn_{2/3}O_2$, the occupancies of the transition metal site were assumed to remain the same as those observed in the pristine material.[19,21]

When the compounds were charged to 4.3 V, 2% of the P3 phase is converted to the O3 phase in Air-$Na_{0.67}Mg_{0.2}Mn_{0.8}O_2$ while the P3 phase is retained in Oxy-$Na_{0.67}Mg_{0.2}Mn_{0.8}O_2$ (Figure 9g). The number of deintercalated Na ions is 0.25 per formula unit for both compounds based on the refinement results, which is smaller than those determined by the charge capacity (removal of 0.44 and 0.35 Na^+ for Air-$Na_{0.67}Mg_{0.2}Mn_{0.8}O_2$ and Oxy-$Na_{0.67}Mg_{0.2}Mn_{0.8}O_2$, respectively). This discrepancy is attributable to the decomposition of the electrolyte as confirmed by XPS. The smaller discrepancy associated with Oxy-$Na_{0.67}Mg_{0.2}Mn_{0.8}O_2$ is consistent with the reduced oxidation peak seen in the dQ/dV plot (Figure 5c). Interestingly, even without transition metal vacancies, 98% of the initial phase is maintained. This observation is in contrast to the previous report which demonstrated that P3-type $Na_{2/3}Mg_{1/3}Mn_{2/3}O_2$ is prone to transformation to the O3 structure upon charge above 4.0 V, which then persists upon subsequent discharge to 1.6 V rather than undergoing a reversible two-phase reaction from O3 to P3. Discharge to 1.8 V after charge to 3.8 V allows more Na ions to intercalate (Figure 9h), leading to a major conversion to an O'3 phase with 11% and 18% P3 phase remaining for Air-$Na_{0.67}Mg_{0.2}Mn_{0.8}O_2$ and Oxy-$Na_{0.67}Mg_{0.2}Mn_{0.8}O_2$, respectively. Refinement of the sodium occupancy in the O'3 phase gave values close to unity in all cases. As a result, the sodium content was fixed at 1 for the final refinements. The ratio between lattice parameters *a* and *b* (*a/b*) in the monoclinic lattice is about 1.87, significantly greater than $\sqrt{3}$, consistent with the expected Jahn-Teller distortion.[28] As shown in the rate performance data for Air-$Na_{0.67}Mg_{0.2}Mn_{0.8}O_2$, the phase transformation in the lower voltage region (P3 to O'3) is sufficiently reversible to deliver stable cycling performance at rates of 10, 50 and 200 mA g^{-1}. The P3 to O'3 phase transformation occurs to minimize the Coulombic repulsion between Na and Mn cations.[28] The presence of vacancies in the transition metal layers may be able to stabilize the trigonal prismatic coordination of NaO_6 via □-Na^+-□ Coulombic attraction. In consequence,

Oxy-$Na_{0.67}Mg_{0.2}Mn_{0.8}O_2$ with vacancies in the transition metal sites exhibits greater structural reversibility within the P3 phase, which remains stable to higher sodium contents. The beneficial effect is considerable when the materials are cycled in the voltage range 1.8-4.3 V. At the end of discharge, significantly reduced phase transformation to the O'3 phase (43 %) is observed with 57 % P3 phase remaining for Oxy-$Na_{0.67}Mg_{0.2}Mn_{0.8}O_2$ whereas 86% O'3 is observed in Air-$Na_{0.67}Mg_{0.2}Mn_{0.8}O_2$.

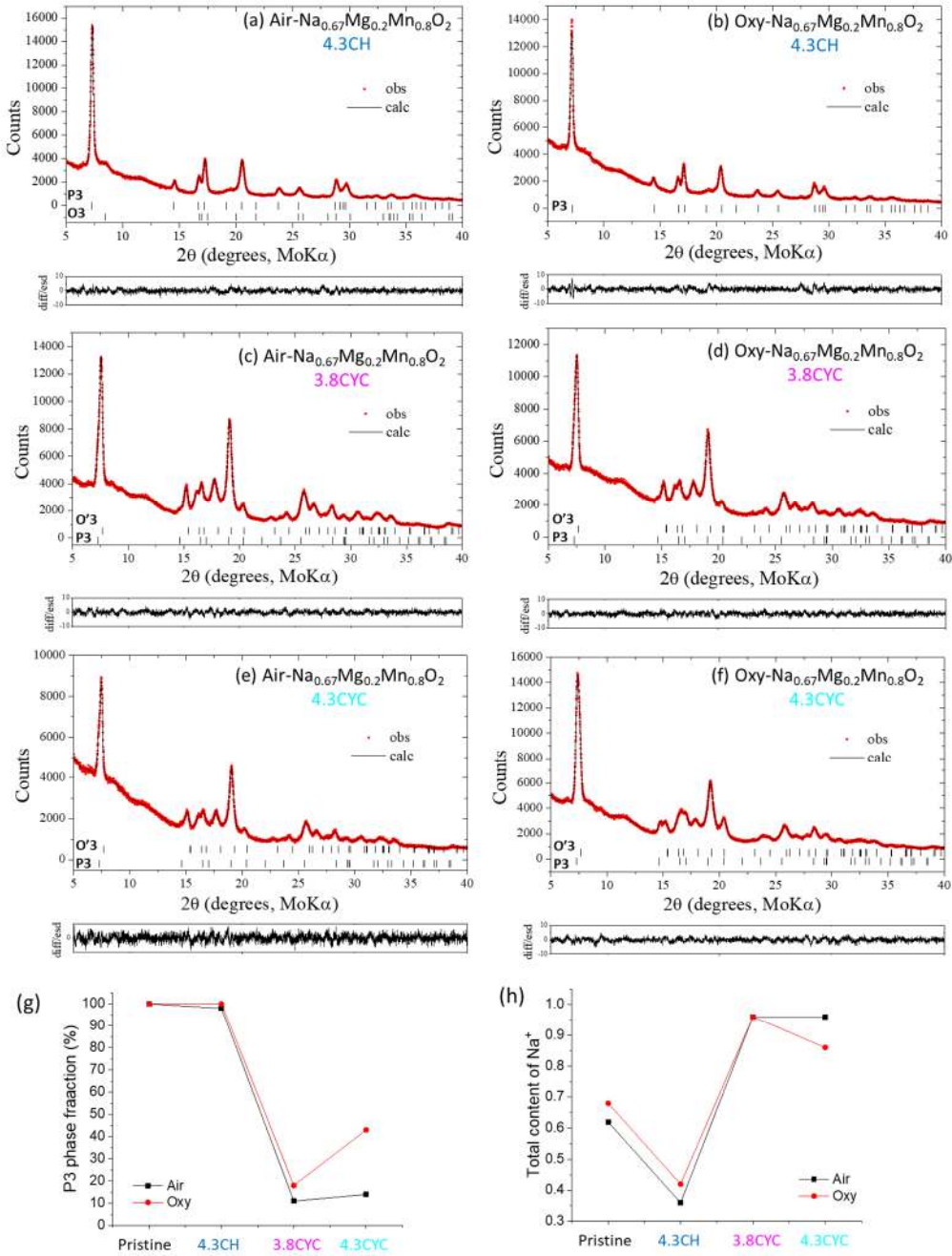

Figure 9. Profile fits for Rietveld refinements of Air-$Na_{0.67}Mg_{0.2}Mn_{0.8}O_2$ (a) charged to 4.3 V, (c) cycled between 1.8-3.8 V and (e) cycled between 1.8-4.3 V. Oxy-$Na_{0.67}Mg_{0.2}Mn_{0.8}O_2$ (b) charged to 4.3 V, (d) cycled between 1.8-3.8 V and (f) cycled between 1.8-4.3 V. Observed data points are shown in red,

with fitted profile in black. Tick marks indicate allowed reflections. (g) P3 phase fraction and (h) total content of Na ion at different states of charge.

Discussion

Considering the similarity in the crystal structure between P3-type Oxy-$Na_{0.67}Mg_{0.2}Mn_{0.8}O_2$ and $Na_{4/7}[\square_{1/7}Mn_{6/7}]O_2$, crystallizing in the triclinic space group $P\bar{1}$ where the edge-sharing MnO_6 octahedra build up $\square_{1/7}Mn_{6/7}O_2$ layers with the ordering between vacancies and Mn ions and sodium ions located between the layers,[45] the novel oxygen redox mechanism exclusively found in Oxygen-$Na_{0.67}Mg_{0.2}Mn_{0.8}O_2$ can be reconciled with previously reported studies on $Na_{4/7}[\square_{1/7}Mn_{6/7}]O_2$. The non-bonding oxygen 2p states generated along Na^+-O-$\square$ or $\square$-O-$\square$ participate in the reversible oxygen redox in this compound.[19,20] The absence of large voltage hysteresis is one of the primary characteristics of anion redox in $Na_{4/7}[\square_{1/7}Mn_{6/7}]O_2$ and recently this phenomenon was explained by the well-maintained oxygen stacking sequence without gliding of $\square_{1/7}Mn_{6/7}O_2$ layers and Mn migration from octahedral sites in the transition metal layers to tetrahedral sites in Na ion layers.[21] In addition, the ordered vacancies in the material permit the stable structure in the bulk as well as on the surface thanks to Coulombic attraction between Na ions and transition metal vacancies.[21] Vacancies on Mn sites in $Na_{0.653}Mn_{0.929}O_2$ which adopts the P2 structure also exhibit oxygen redox with an obvious voltage plateau at about 4.2 V.[29] There are general rules that permit the rationalization of the effects of unhybridized O 2p states on reversible oxygen redox in LIBs.[46] Based on the observations in the current study and those of previous studies,[19–21,29,46] we propose that two different oxygen redox mechanisms occur in Oxy-$Na_{0.67}Mg_{0.2}Mn_{0.8}O_2$ associated with the presence of transition metal vacancies and the substituted Mg. The former is triggered at slightly higher voltage than the latter and is reversible with a notably narrow polarization due to the retention of the P3 structure at the end of charge to 4.3 V. The oxidized oxygen originating from the unpaired O 2p states created by substituted Mg is then reduced at a significantly lower voltage, resulting in large voltage hysteresis.

CONCLUSIONS

The P3-type Air-$Na_{0.67}Mg_{0.2}Mn_{0.8}O_2$ and Oxygen-$Na_{0.67}Mg_{0.2}Mn_{0.8}O_2$ show stable cycling performance in the voltage range 1.8-3.8 V where the electrochemical reaction is entirely based on the Mn^{3+}/Mn^{4+} redox couple. Over the wider voltage window from 1.8 to 4.3 V, both compounds exhibit oxygen redox in the high voltage region. The limited oxygen redox based solely on the substituted Mg for Air-$Na_{0.67}Mg_{0.2}Mn_{0.8}O_2$ is extended for Oxygen-$Na_{0.67}Mg_{0.2}Mn_{0.8}O_2$ by a further decoupled mechanism based on transition metal vacancies. The presence of vacancies in the transition metal layers for P3-type $Na_{0.67}Mg_{0.2}Mn_{0.8}O_2$ not only provides a reversible oxygen redox couple but also preserves the P3 structure over several cycles.

ASSOCIATED CONTENT

Supporting Information

PXRD refinement results, electrochemical data, XANES data

AUTHOR INFORMATION

Corresponding Author

*E-mail: ara@st-andrews.ac.uk

ACKNOWLEDGEMENT

REFERENCES

(1)   Mortemard De Boisse, B.; Liu, G.; Ma, J.; Nishimura, S. I.; Chung, S. C.; Kiuchi, H.; Harada, Y.; Kikkawa, J.; Kobayashi, Y.; Okubo, M.; Yamada, A. Intermediate Honeycomb Ordering to Trigger Oxygen Redox Chemistry in Layered Battery Electrode. *Nat. Commun.* **2016**, *7*, 11397–11406. https://doi.org/10.1038/ncomms11397.

(2)   Perez, A. J.; Batuk, D.; Saubanère, M.; Rousse, G.; Foix, D.; McCalla, E.; Berg, E. J.; Dugas, R.; Van Den Bos, K. H. W.; Doublet, M. L.; Gonbeau, D.; Abakumov, A. M.; Van Tendeloo, G.; Tarascon, J. M. Strong Oxygen Participation in the Redox Governing the Structural and Electrochemical Properties of Na-Rich Layered Oxide Na_2IrO_3. *Chem. Mater.* **2016**, *28*, 8278–8288. https://doi.org/10.1021/acs.chemmater.6b03338.

(3)   Yabuuchi, N.; Kajiyama, M.; Iwatate, J.; Nishikawa, H.; Hitomi, S.; Okuyama, R.; Usui, R.; Yamada, Y.; Komaba, S. P2-Type $Na_x[Fe_{1/2}Mn_{1/2}]O_2$ Made from Earth-Abundant Elements for Rechargeable Na Batteries. *Nat. Mater.* **2012**, *11*, 512–517. https://doi.org/10.1038/nmat3309.

(4)   Yabuuchi, N.; Hara, R.; Kubota, K.; Paulsen, J.; Kumakura, S.; Komaba, S. A New Electrode Material for Rechargeable Sodium Batteries: P2-Type $Na_{2/3}[Mg_{0.28}Mn_{0.72}]O_2$ with Anomalously High Reversible Capacity. *J. Mater. Chem. A* **2014**, *2*, 16851–16855. https://doi.org/10.1039/c4ta04351k.

(5)   Yabuuchi, N.; Hara, R.; Kajiyama, M.; Kubota, K.; Ishigaki, T.; Hoshikawa, A.; Komaba, S. New O2/P2-Type Li-Excess Layered Manganese Oxides as Promising Multi-Functional Electrode Materials for Rechargeable Li/Na Batteries. *Adv. Energy Mater.* **2014**, *4*, 1301453–1301476. https://doi.org/10.1002/aenm.201301453.

(6)   De La Llave, E.; Talaie, E.; Levi, E.; Nayak, P. K.; Dixit, M.; Rao, P. T.; Hartmann, P.; Chesneau, F.; Major, D. T.; Greenstein, M.; Aurbach, D.; Nazar, L. F. Improving Energy Density and Structural Stability of Manganese Oxide Cathodes for Na-Ion Batteries by Structural Lithium Substitution. *Chem. Mater.* **2016**, *28*, 9064–9076. https://doi.org/10.1021/acs.chemmater.6b04078.

(7)   Ma, C.; Alvarado, J.; Xu, J.; Clément, R. J.; Kodur, M.; Tong, W.; Grey, C. P.; Meng, Y. S. Exploring Oxygen Activity in the High Energy P2-Type $Na_{0.78}Ni_{0.23}Mn_{0.69}O_2$ Cathode Material for Na-Ion Batteries. *J. Am. Chem. Soc.* **2017**, *139*, 4835–4845. https://doi.org/10.1021/jacs.7b00164.

(8)   Bai, X.; Sathiya, M.; Mendoza-Sánchez, B.; Iadecola, A.; Vergnet, J.; Dedryvère, R.; Saubanère, M.; Abakumov, A. M.; Rozier, P.; Tarascon, J. M. Anionic Redox Activity in a Newly Zn-Doped Sodium Layered Oxide P2-$Na_{2/3}Mn_{1-y}Zn_yO_2$ ($0 < y < 0.23$). *Adv. Energy Mater.* **2018**, *8*, 1802379–1802391. https://doi.org/10.1002/aenm.201802379.

(9)   Maitra, U.; House, R. A.; Somerville, J. W.; Tapia-Ruiz, N.; Lozano, J. G.; Guerrini, N.; Hao, R.; Luo, K.; Jin, L.; Pérez-Osorio, M. A.; Massel, F.; Pickup, D. M.; Ramos, S.; Lu, X.; McNally, D. E.; Chadwick, A. V.; Giustino, F.; Schmitt, T.; Duda, L. C.; Roberts, M. R.; Bruce, P. G. Oxygen Redox Chemistry without Excess Alkali-Metal Ions in $Na_{2/3}[Mg_{0.28}Mn_{0.72}]O_2$. *Nat. Chem.* **2018**, *10*, 288–295. https://doi.org/10.1038/nchem.2923.

(10)   Du, K.; Zhu, J.; Hu, G.; Gao, H.; Li, Y.; Goodenough, J. B. Exploring Reversible Oxidation of Oxygen in a Manganese Oxide. *Energy Environ. Sci.* **2016**, *9*, 2575–2577. https://doi.org/10.1039/c6ee01367h.

(11)   Rong, X.; Liu, J.; Hu, E.; Liu, Y.; Wang, Y.; Wu, J.; Yu, X.; Page, K.; Hu, Y. S.; Yang, W.; Li, H.; Yang, X. Q.; Chen, L.; Huang, X. Structure-Induced Reversible Anionic Redox Activity in Na Layered Oxide Cathode. *Joule* **2018**, *2*, 125–140. https://doi.org/10.1016/j.joule.2017.10.008.

(12)   Song, B.; Hu, E.; Liu, J.; Zhang, Y.; Yang, X. Q.; Nanda, J.; Huq, A.; Page, K. A Novel P3-Type $Na_{2/3}Mg_{1/3}Mn_{2/3}O_2$ as High Capacity Sodium-Ion Cathode Using Reversible Oxygen Redox. *J. Mater. Chem. A* **2019**, *7*, 1491–1498. https://doi.org/10.1039/c8ta09422e.

(13)   Kim, E. J.; Ma, L. A.; Duda, L. C.; Pickup, D. M.; Chadwick, A. V.; Younesi, R.; Irvine, J. T. S.; Armstrong, A. R. Oxygen Redox Activity through a Reductive Coupling Mechanism in the P3-Type Nickel-Doped Sodium Manganese Oxide. *ACS Appl. Energy Mater.* **2020**, *3*, 184–191. https://doi.org/10.1021/acsaem.9b02171.

(14)   Gent, W. E.; Lim, K.; Liang, Y.; Li, Q.; Barnes, T.; Ahn, S. J.; Stone, K. H.; McIntire, M.; Hong, J.; Song, J. H.; Li, Y.; Mehta, A.; Ermon, S.; Tyliszczak, T.; Kilcoyne, D.; Vine, D.; Park, J. H.; Doo, S. K.; Toney, M. F.; Yang, W.; Prendergast, D.; Chueh, W. C. Coupling between Oxygen Redox and Cation Migration Explains Unusual Electrochemistry in Lithium-Rich Layered Oxides. *Nat. Commun.* **2017**, *8*, 1-12. https://doi.org/10.1038/s41467-017-02041-x.

(15)   Assat, G.; Tarascon, J. M. Fundamental Understanding and Practical Challenges of Anionic Redox Activity in Li-Ion Batteries. *Nat. Energy* **2018**, *3*, 373–386. https://doi.org/10.1038/s41560-018-0097-0.

(16)   Chen, C. J.; Pang, W. K.; Mori, T.; Peterson, V. K.; Sharma, N.; Lee, P. H.; Wu, S. H.; Wang, C. C.; Song, Y. F.; Liu, R. S. The Origin of Capacity Fade in the $Li_2MnO_3 \cdot LiMO_2$ (M = Li, Ni, Co, Mn) Microsphere Positive Electrode: An Operando Neutron Diffraction and Transmission X-Ray Microscopy Study. *J. Am. Chem. Soc.* **2016**, *138*, 8824–8833. https://doi.org/10.1021/jacs.6b03932.

(17) Armstrong, A. R.; Dupre, N.; Paterson, A. J.; Grey, C. P.; Bruce, P. G. Combined Neutron Diffraction, NMR, and Electrochemical Investigation of the Layered-to-Spinel Transformation in $LiMnO_2$. *Chem. Mater.* **2004**, *16*, 3106–3118. https://doi.org/10.1021/cm034964b.

(18) House, R. A.; Maitra, U.; Jin, L.; Lozano, J. G.; Somerville, J. W.; Rees, N. H.; Naylor, A. J.; Duda, L. C.; Massel, F.; Chadwick, A. V.; Ramos, S.; Pickup, D. M.; McNally, D. E.; Lu, X.; Schmitt, T.; Roberts, M. R.; Bruce, P. G. What Triggers Oxygen Loss in Oxygen Redox Cathode Materials? *Chem. Mater.* **2019**, *31*, 3293–3300. https://doi.org/10.1021/acs.chemmater.9b00227.

(19) Mortemard de Boisse, B.; Nishimura, S. ichi; Watanabe, E.; Lander, L.; Tsuchimoto, A.; Kikkawa, J.; Kobayashi, E.; Asakura, D.; Okubo, M.; Yamada, A. Highly Reversible Oxygen-Redox Chemistry at 4.1 V in $Na_{4/7-x}[\square_{1/7}Mn_{6/7}]O_2$ ($\square$: Mn Vacancy). *Adv. Energy Mater.* **2018**, *8*, 1800409–1800416. https://doi.org/10.1002/aenm.201800409.

(20) Li, Y.; Wang, X.; Gao, Y.; Zhang, Q.; Tan, G.; Kong, Q.; Bak, S.; Lu, G.; Yang, X.-Q.; Gu, L.; Lu, J.; Amine, K.; Wang, Z.; Chen, L. Native Vacancy Enhanced Oxygen Redox Reversibility and Structural Robustness. *Adv. Energy Mater.* **2019**, *9*, 1803087–1803096. https://doi.org/10.1002/aenm.201803087.

(21) Song, B.; Tang, M.; Hu, E.; Borkiewicz, O. J.; Wiaderek, K. M.; Zhang, Y.; Phillip, N. D.; Liu, X.; Shadike, Z.; Li, C.; Song, L.; Hu, Y. Y.; Chi, M.; Veith, G. M.; Yang, X. Q.; Liu, J.; Nanda, J.; Page, K.; Huq, A. Understanding the Low-Voltage Hysteresis of Anionic Redox in $Na_2Mn_3O_7$. *Chem. Mater.* **2019**, *31*, 3756–3765. https://doi.org/10.1021/acs.chemmater.9b00772.

(22) Toby, B. H. EXPGUI, a Graphical User Interface for GSAS. *J. Appl. Crystallogr.* **2001**, *34*, 210–213. https://doi.org/10.1107/S0021889801002242.

(23) Coelho, A. A. Whole-Profile Structure Solution from Powder Diffraction Data Using Simulated Annealing. *J. Appl. Crystallogr.* **2000**, *33*, 899–908. https://doi.org/10.1107/S002188980000248X.

(24) Ashley, J. C. Energy Losses and Inelastic Mean Free Paths of Low-Energy Electrons in Polyethylene. *Radiat. Res.* **1982**, *90*, 433–436. https://doi.org/https://doi.org/10.2307/3575717.

(25) Armstrong, A. R.; Paterson, A. J.; Robertson, A. D.; Bruce, P. G. Nonstoichiometric Layered $Li_xMn_yO_2$ with a High Capacity for Lithium Intercalation/Deintercalation. *Chem. Mater.* **2002**, *14*, 710–719. https://doi.org/10.1021/cm010382n.

(26) Robertson, A. D.; Armstrong, A. R.; Paterson, A. J.; Duncan, M. J.; Bruce, P. G. Nonstoichiometric

Layered $Li_xMn_yO_2$ Intercalation Electrodes - A Multiple Dopant Strategy. *J. Mater. Chem.* **2003**, *13*, 2367–2373. https://doi.org/10.1039/b302245e.

(27) Robertson, A. D.; Armstrong, A. R.; Bruce, P. G. Layered $Li_xMn_{1-y}Co_yO_2$ Intercalation Electrodes - Influence of Ion Exchange on Capacity and Structure upon Cycling. *Chem. Mater.* **2001**, *13*, 2380–2386. https://doi.org/10.1021/cm000965h.

(28) Parant, J. P.; Olazcuaga, R.; Devalette, M.; Fouassier, C.; Hagenmuller, P. Sur Quelques Nouvelles Phases de Formule Na_xMnO_2 (x ≤ 1). *J. Solid State Chem.* **1971**, *3*, 1–11. https://doi.org/10.1016/0022-4596(71)90001-6.

(29) Zhao, C.; Wang, Q.; Lu, Y.; Jiang, L.; Liu, L.; Yu, X.; Chen, L.; Li, B.; Hu, Y. S. Decreasing Transition Metal Triggered Oxygen Redox Activity in Na-Deficient Oxides. *Energy Storage Mater.* **2019**, *20*, 395–400. https://doi.org/10.1016/j.ensm.2018.10.025.

(30) Wang, X.; Tamaru, M.; Okubo, M.; Yamada, A. Electrode Properties of P2 − $Na_{2/3}Mn_yCo_{1-y}O_2$ as Cathode Materials for Sodium-Ion Batteries. *J. Phys. Chem. C* **2013**, *117*, 15545–15551. https://doi.org/10.1021/jp406433z.

(31) Billaud, J.; Singh, G.; Armstrong, A. R.; Gonzalo, E.; Roddatis, V.; Armand, M.; Rojo, T.; Bruce, P. G. $Na_{0.67}Mn_{1-x}Mg_xO_2$ (0 ≤ x ≤ 0.2): A High Capacity Cathode for Sodium-Ion Batteries. *Energy Environ. Sci.* **2014**, *7*, 1387–1391. https://doi.org/10.1039/c4ee00465e.

(32) Thackeray, M. M. Manganese Oxides for Lithium Batteries. *Prog. Solid State Chem.* **1997**, *25*, 1–71. https://doi.org/10.1016/s0079-6786(97)81003-5.

(33) Bruce, P. G. *Solid State Electrochemistry*; Cambridge University Press, 2003.

(34) Yabuuchi, N.; Kubota, K.; Dahbi, M.; Komaba, S. Research Development on Sodium-Ion Batteries. *Chem. Rev.* **2014**, *114*, 11636–11682. https://doi.org/10.1021/cr500192f.

(35) House, R. A.; Maitra, U.; Pérez-Osorio, M. A.; Lozano, J. G.; Jin, L.; Somerville, J. W.; Duda, L. C.; Nag, A.; Walters, A.; Zhou, K.-J.; Roberts, M. R.; Bruce, P. G. Superstructure Control of First-Cycle Voltage Hysteresis in Oxygen-Redox Cathodes. *Nature* **2020**, *577*, 502–508. https://doi.org/10.1038/s41586-019-1854-3.

(36) Manceau, A.; Marcus, M. A.; Grangeon, S. Determination of Mn Valence States in Mixed-Valent Manganates by XANES Spectroscopy. *Am. Mineral.* **2012**, *97*, 816–827. https://doi.org/10.2138/am.2012.3903.

(37) Kim, E. J.; Pickup, D. M.; Chadwick, A. V.; Irvine, J. T. S.; Mofredj, K.; Armstrong, A. R. Activation

of Anion Redox in P3 Structure $Na_{0.6}Co_{0.2}Mn_{0.8}O_2$ via Introduction of Transition Metal Vacancies. under review.

(38)   Kim, E. J.; Armstrong, A. R. Unpublished Results.

(39)   Kubota, K.; Komaba, S. Review-Practical Issues and Future Perspective for Na-Ion Batteries. *J. Electrochem. Soc.* **2015**, *162*, A2538–A2550. https://doi.org/10.1149/2.0151514jes.

(40)   Yabuuchi, N.; Yoshii, K.; Myung, S. T.; Nakai, I.; Komaba, S. Detailed Studies of a High-Capacity Electrode Material for Rechargeable Batteries, Li_2MnO_3-$LiCo_{1/3}Ni_{1/3}Mn_{1/3}O_2$. *J. Am. Chem. Soc.* **2011**, *133*, 4404–4419. https://doi.org/10.1021/ja108588y.

(41)   Björklund, E.; Brandell, D.; Hahlin, M.; Edström, K.; Younesi, R. How the Negative Electrode Influences Interfacial and Electrochemical Properties of $LiNi_{1/3}Co_{1/3}Mn_{1/3}O_2$ Cathodes in Li-Ion Batteries. *J. Electrochem. Soc.* **2017**, *164*, A3054–A3059. https://doi.org/10.1149/2.0711713jes.

(42)   Gieu, J. B.; Winkler, V.; Courrèges, C.; El Ouatani, L.; Tessier, C.; Martinez, H. New Insights into the Characterization of the Electrode/Electrolyte Interfaces within $LiMn_2O_4$/$Li_4Ti_5O_{12}$cells, by X-Ray Photoelectron Spectroscopy, Scanning Auger Microscopy and Time-of-Flight Secondary Ion Mass Spectrometry. *J. Mater. Chem. A* **2017**, *5*, 15315–15325. https://doi.org/10.1039/c7ta02529g.

(43)   Eshetu, G. G.; Elia, G. A.; Armand, M.; Forsyth, M.; Komaba, S.; Rojo, T.; Passerini, S. Electrolytes and Interphases in Sodium-Based Rechargeable Batteries: Recent Advances and Perspectives. *Adv. Energy Mater.* **2020**. *10,* 2000093-2000134 https://doi.org/10.1002/aenm.202000093.

(44)   Mortemard de Boisse, B.; Reynaud, M.; Ma, J.; Kikkawa, J.; Nishimura, S. ichi; Casas-Cabanas, M.; Delmas, C.; Okubo, M.; Yamada, A. Coulombic Self-Ordering upon Charging a Large-Capacity Layered Cathode Material for Rechargeable Batteries. *Nat. Commun.* **2019**, *10*, 2185–2782. https://doi.org/10.1038/s41467-019-09409-1.

(45)   Adamczyk, E.; Pralong, V. $Na_2Mn_3O_7$: A Suitable Electrode Material for Na-Ion Batteries? *Chem. Mater.* **2017**, *29* , 4645–4648. https://doi.org/10.1021/acs.chemmater.7b01390.

(46)   Seo, D. H.; Lee, J.; Urban, A.; Malik, R.; Kang, S.; Ceder, G. The Structural and Chemical Origin of the Oxygen Redox Activity in Layered and Cation-Disordered Li-Excess Cathode Materials. *Nat. Chem.* **2016**, *8*, 692–697. https://doi.org/10.1038/nchem.2524.

TABLE OF CONTENTS